This is a “preproof” accepted article for *Mineralogical Magazine*.
This version may be subject to change during the production process.
10.1180/mgm.2025.27

Yamhamelachite, $KCrP_2O_7$, a new natural pyrophosphate from phosphide-bearing breccia of the Hatrurim Complex, Negev Desert, Israel

Evgeny V. Galuskin[1]*, Joachim Kusz[2], Irina O. Galuskina[1], Yevgeny Vapnik[3] and Grzegorz Zieliński[4]

[1]Institute of Earth Sciences, Faculty of Natural Sciences, University of Silesia, Będzińska 60, 41-200 Sosnowiec, Poland

[2]Faculty of Science and Technology, University of Silesia, 75. Pułku Piechoty 1, 41-500 Chorzów, Poland

[3]Department of Geological and Environmental Sciences, Ben-Gurion University of the Negev, P.O.B. 653, Beer-Sheva 84105, Israel

[4]Polish Geological Institute – National Research Institute, Rakowiecka 4, 00-975 Warsaw, Poland.

*E-mail: evgeny.galuskin@us.edu.pl

Abstract

Phosphide-bearing diopside-anorthite paralava found in the distribution area of the pyrometamorphic rocks of the Hatrurim Complex in Jordan (Daba-Siwaqa field) and Israel (Hatrurim Basin field) have yielded a large number of new phosphides and phosphates. In 2019, a small outcrop of phosphide-bearing breccia with cement composed of gehlenite-flamite paralava was discovered in the Hatrurim Basin. A new pyrophosphate, yamhamelachite, $KCrP_2O_7$ ($P2_1/c$, a = 7.3574(3), b = 9.9336(4), c = 8.1540(4) Å, β = 106.712(5)°, V = 570.77(5)Å^3, Z = 4), occurs at the phosphide-enriched boundary between an altered sedimentary xenolith and the gehlenite-flamite paralava. Yamhamelachite forms green aggregates in which the size of grains does not exceed 25-30 μm. The mineral is transparent with a glassy lustre. Yamhamelachite is brittle with conchoidal fracture. Mohs hardness = 4. The empirical formula of yamhamelachite calculated on the basis of average microprobe analyses is $(K_{0.89}Ca_{0.01}\square_{0.10})_{\sum 1.00}Cr^{3+}_{0.50}V^{3+}_{0.33}Al_{0.15}Fe^{3+}_{0.04}Ti^{4+}_{0.03})_{\sum 1.05}P_{1.98}O_7$. The density calculated from the empirical formula and structural data is 3.035 g·cm^{-3}. Cr^{3+} in yamhamelachite is substituted by V^{3+}, and in a few cases V is marginally more abundant than Cr, indicating the presence of a potentially new mineral with the formula KVP_2O_7. Yamhamelachite consists of layers of Cr^{3+}-octahedra and pyrophosphate groups connected at their apices, and potassium located within channels parallel to [001]. A characteristic feature

https://doi.org/10.1180/mgm.2025.27 Published online by Cambridge University Press

of phosphide aggregates associated with yamhamelachite is the presence of two generations of barringerite, the earlier of which has higher Cr and V content. In the general crystallisation sequence, yamhamelachite appears after phosphides (+pyrrhotite, daubréelite) and then spinels of the chromite-magnetite series crystallise, along with ferromerrillite and ferroalluaudite. The source of chromium for yamhamelachite was mainly V-Cr-bearing pyrrhotite and V-bearing daubréelite. The low Fe^{3+} content in yamamelachite, likely related to its late-stage alteration, indicates that it crystallised from phosphate melt under reducing conditions at ~1000°C.

Keywords: yamhamelachite, new mineral, pyrophosphate, structure, Raman, barringerrite, pyrometamorphic rock, Hatrurim Complex, Israel

Introduction

Yamhamelachite, $KCrP_2O_7$, is the first natural anhydrous large-cation pyrophosphate found in phosphide-bearing breccia in the Hatrurim Basin, Negev Desert, Israel. It has a synthetic analogue (Gentil *et al*., 1997) which belongs to the $KAlP_2O_7$ structural archetype (Ng and Calvo, 1973).

In the last decade, a large number of new Ca, Fe, and Ni phosphates have been found in pyrometamorphic rocks of the Hatrurim Complex (Daba-Siwaqa, Jordan and Hatrurim Basin, Negev Desert, Israel), including 5 pyrophosphates: anastasenkoite, $CaFe^{2+}(P_2O_7)$; lisanite, $CaNiP_2O_7$; nabateaite, $Fe^{2+}P_2O_7$; samraite, $Ni_2P_2O_7$, and shasuite, $CaNi_3(P_2O_7)_2$ (Britvin *et al*., 2020a, 2021a,b,c,d). In addition, cyclophosphates, namely phosphocyclite-(Fe) and phosphocyclite-(Ni) have been discovered in nature for the first time (Britvin *et al*., 2021e). These phosphates, and associated Fe and Ni phosphides, are confined to the contact between the diopside-bearing paralava and the thermally altered clay-carbonate host sedimentary rock of the Ghareb Formation. Interestingly, all of the above phosphates have been described from a single sample found *ex situ* in the Halamish Wadi, Hatrurim Basin, Negev Desert, Israel.

In this paper we describe the composition and structure of a new mineral, yamhamelachite. Yamhamelachite was found in an outcrop on the side of the Arad-Dead Sea road, Israel. Its name is derived from the Hebrew for the *Dead Sea*: Yam Ha-Melach (מלח ים, the Sea of Salt). Type material has been deposited in the mineralogical collection of the Fersman Mineralogical Museum, Leninskiy pr., 18/k. 2, 119071 Moscow, Russia, registration number: 6074/1. We also present the results of a study of the composition of minerals

https://doi.org/10.1180/mgm.2025.27 Published online by Cambridge University Press

associated with yamhamelachite and the results of structural studies of two generations of barringerite. The paper discusses the formation of phosphides and phosphates at the boundary of heated paralava and altered sedimentary rock fragments.

Methods of investigation

The morphology and chemical composition of yamhamelachite, phosphides and associated minerals were studied using Phenom XL and Quanta 250 EDS-equipped scanning electron microscopes (Institute of Earth Sciences, University of Silesia, Poland). Mineral chemical composition was measured with a Cameca SX100 electron microprobe analyzer (EMPA, Micro-Area Analysis Laboratory, Polish Geological Institute—National Research Institute, Warsaw, Poland): WDS, acceleration voltage = 15 kV, beam current = 20 nA (phosphates, sulfides) or 40 nA (phosphides), and beam diameter ~1 μm. The following standards and lines were used: albite = Na*K*α, apatite = Ca*K*α, P*K*α; celestine = Sr*L*α, chalcopyrite = Cu*K*α, diopside = Mg*K*α, orthoclase = K*K*α and Al*K*α; pentlandite = Fe*K*α, Ni*K*α, S*K*α; rutile = Ti*K*α; V metal = V*K*α; Cr_2O_3 = Cr*K*α, wollastonite = Si*K*α.

Raman spectra of yamhamelachite were recorded on a WITec alpha 300R Confocal Raman Microscope (Department of Earth Science, University of Silesia, Poland) equipped with an air-cooled solid state laser (532 nm) and a CCD camera. An air Zeiss LD EC Epiplan-Neofluan DIC-100/0.75NA objective was used. The Raman scattered light was focused onto a multi-mode fibre and a monochromator with an 1800 mm^{-1} grating. The laser power at the sample position was ~20 mW. 15 scans with an integration time of 3 s and a resolution of 1.5 cm^{-1} were collected and averaged.

Single-crystal X-ray studies of yamhamelachite and barringerite were performed using a SuperNova diffractometer with a mirror monochromator [Cu*K*α, λ = 1.54184 Å (yamhamelachite); Mo*K*α, λ = 0.71073 Å (barringerite)] and an Atlas CCD detector (formerly Agilent Technologies, currently Rigaku Oxford Diffraction) at the Institute of Physics, University of Silesia, Poland.

Occurrence and general appearance

High-temperature pyrometamorphic rocks of the Hatrurim Complex and their alteration products are widely distributed along the Dead Sea rift in the territories of Israel, Palestine and Jordan. The most typical rocks are spurrite marble, larnite pseudoconglomerate and gehlenite hornfels (Bentor, 1960; Gross, 1977; Vapnik *et al*., 2007; Novikov *et al*., 2013).

https://doi.org/10.1180/mgm.2025.27 Published online by Cambridge University Press

The highest temperature rocks of the Complex are paralavas of various types, most of which comprise oxidised mineral associations (Galuskina *et al*., 2017). The rarest type encompasses diopside-bearing and gehlenite-bearing reduced paralavas, which are associated with the presence of phosphides (Britvin *et al*., 2015; Galuskin *et al*., 2023a,b, 2024a).

Yamhamelachite was discovered in phosphide-bearing breccia found in 2019 in the Hatrurim Basin on the artificial outcrop formed as a result of the construction of the Arad-Dead Sea road. The geological description of this unique and highly inhomogeneous breccia with cement composed of gehlenite-flamite (±rankinite, pseudowollastonite) paralava can be found in a number of our papers alongside descriptions of minerals previously known only from meteorites, such as osbornite, allabogdanite, dmitryivanovite, grokhovskyite, caswellsilverite and rubinite (Galuskin *et al*., 2022, 2023a,b, 2024a).

Yamhamelachite is a rare mineral in the breccia and forms thin zones of 2–3 μm on zonal aggregates of phosphides with the following zonation: barringerite → schreibersite → eutectica: schreibersite+native iron (Fig. 1). Phosphides are concentrated at the boundary of the paralava and thermally altered sedimentary xenoliths (Fig. 2a). Inclusions of Cr-V-bearing pyrrhotite are often noted at the rim of these aggregates (Galuskin *et al*., 2022). The occurrence of late-generation barringerite, replacing schreibersite, and its association with minerals of the merrillite subgroup and fluorapatite is a characteristic feature of phosphide aggregates with yamhamelachite (Fig. 1b).

In one case, a zone of yamhamelachite up to 30 μm thick was found in the hematite aggregate formed after pyrrhotite (Fig. 2), which was the source of grains for single-crystal structural and optical studies. Next to this yamhamelachite excretion (Fig. 2a) is a zoned aggregate: barringerite I → eutectic: schreibersite+barringerite → barringerite II → yamhamelachite → chromite+magnetite → ferromerrillite (Fig. 3). The eutectic zone contains daubréelite inclusions, and partially oxidised pyrrhotite inclusions were noted in barringerite II (Fig. 3b). As ‘barringerite I’ and ‘barringerite II’ could have different structures—hexagonal (barringerite) or orthorhombic (allabogdanite)—we carried out structural studies using SC-XRD, which confirmed that both generations of Fe_2P minerals correspond to barringerite.

It should be added that pyrrhotite was widespread in the rock, which often had lamellae of Cr and V-enriched pyrrhotite and/or daubréelite (Galuskin *et al*., 2023a). In samples containing yamhamelachite, pyrrhotite was almost completely replaced by hematite,

https://doi.org/10.1180/mgm.2025.27 Published online by Cambridge University Press

forming characteristic framework pseudomorphs reminiscent of the lamellar structure of pyrrhotite (Figs 1b, 2c).

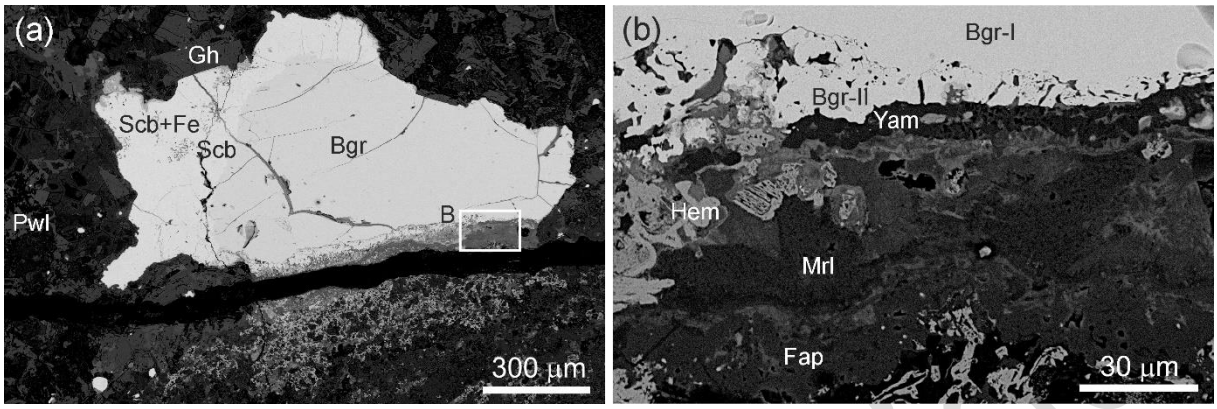

Figure 1. (a) Zonal aggregate of phosphides showing a barringerite-schreibersite-eutectic (schreibersite-native iron) sequence. The fragment magnified in Fig. 1b is shown in the frame. (b) Thin zones of yamhamelachite up to 5 μm thick on zonal aggregates of phosphides containing two generations of barringerite. Bgr – barringerite, Bgr-I – barringerite, generation I; Bgr-II – barringerite, generation II; Gh – gehlenite; Fap – fluorapatite; Fe – native iron; Hem – hematite; Mrl – merrillite, Pwo – pseudowollastonite, Scb – schreibersite, Yam – yamhamelachite.

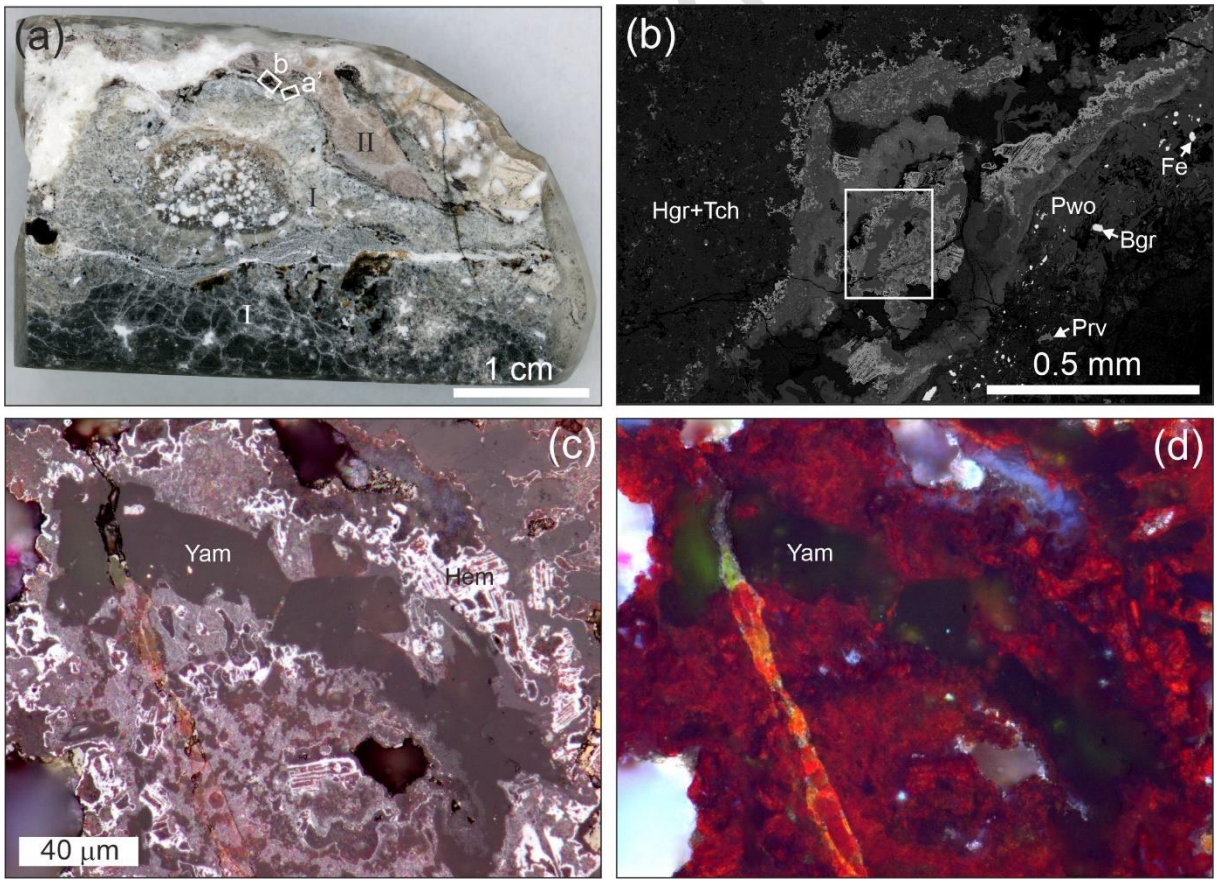

Figure 2. (a) Polished slab of phosphide-bearing breccia. I – paralava, II – altered fragment of sedimentary rock. The frames labelled b and a' indicate the fragments enlarged in Fig. 2b and 3a, respectively. (b) Hematite aggregate formed after pyrrhotite, in which the greatest yamhamelachite deposit was found. The fragment magnified in Fig. 2c is shown in the frame. (c, d) Optical image of yamhamelachite, reflected light, c – PP

https://doi.org/10.1180/mgm.2025.27 Published online by Cambridge University Press

(polarised light), d – XP (cross polarised light). Bgr – barringerite, Fe – native iron; Hem – hematite; Hgr – hydrogrossular, Prv – perovskite, Pwo – pseudowollastonite, Tch – tacharanite, Yam – yamhamelachite.

Yamhamelachite forms dark green granular aggregates in which the grain size does not exceed 25-30 mm (Fig. 2d). The mineral is transparent with a glassy lustre. Yamhamelachite is a brittle mineral with a conchoidal fracture indicating a lack of cleavage. Mohs hardness = 4. The density calculated on the basis of the empirical formula and the structural data is 3.035 $g \cdot cm^{-3}$. Selected yamhamelachite grains are usually very small (~10 μm) and intergrow with Fe-oxides. Therefore, extraction of pure yamhamelachite grain suitable for optical characterization was a challenging task. Only minimal [$\alpha = 1.640(3)$], and maximal [$\gamma = 1.662(3)$] refractive indexes could be measured, but the superior Gladstone-Dale compatibility ($1-(K_P/K_C) = -0.0076$) shows that the measurements are correct.

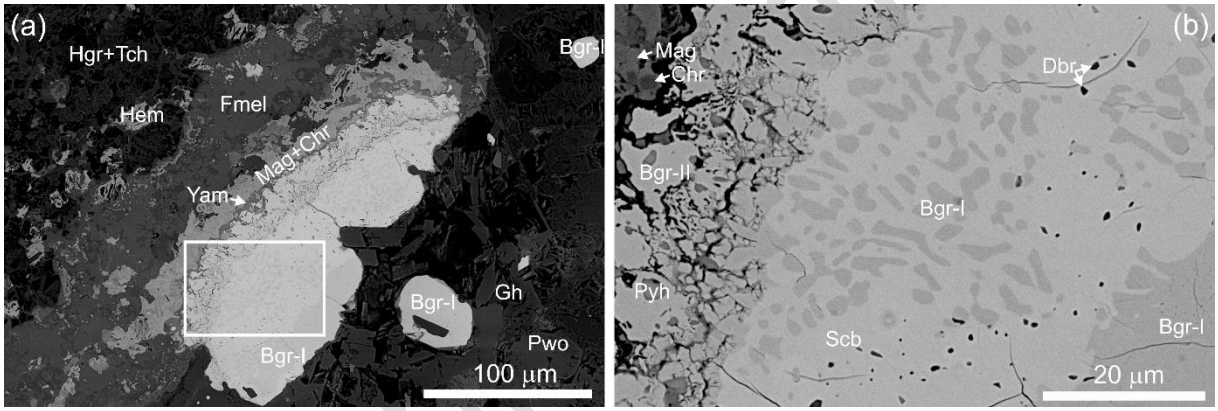

Figure 3. (a) Zonal aggregate of phosphides with edges of Fe-Cr spinels and ferromerrillite. The fragment magnified in Fig. 3b is outlined. (b) In the zonal aggregate of phosphides, the following changes can be observed: barringerite of the I generation → eutectic: schreibersite-barringerite with daubréelite inclusions → barringerite of the II generation replaced by schreibersite with inclusions of Cr-V-bearing pyrrhotite. Bgr-I – barringerite, generation I; Bgr-II – barringerite, generation II; Dbr – daubréelite, Gh – gehlenite; Hem – hematite; Fmel – ferromerrillite, Hgr – hydrogrossular, Mag – magnetite, Chr – chromite, Pyh – pyrrhotite, Pwo – pseudowollastonite, Scb – schreibersite, Tch – tacharanite, Yam – yamhamelachite.

Chemical composition

The empirical formula of yamhamelachite calculated on the basis of average microprobe analyses is $(K_{0.89}Ca_{0.01}\square_{0.10})_{\sum 1.00}Cr^{3+}_{0.50}V^{3+}_{0.33}Al_{0.15}Fe^{3+}_{0.04}Ti^{4+}_{0.03})_{\sum 1.05}P_{1.98}O_7$ (Table 1, an. 1) and contains the main end-members: $KCr^{3+}P_2O_7$ – 50%, $KV^{3+}P_2O_7$ – 33%, $KAlP_2O_7$ – 15%. The maximum chromium content in yamhamelachite is 16.43 wt. % Cr_2O_3, which corresponds to 0.57 Cr pfu (Table 1, an. 2). In rare cases, V > Cr (Table 1, an. 3), and the empirical formula of the mineral becomes $(K_{0.87}\square_{0.13})_{\sum 1.00}(V^{3+}_{0.53}Cr^{3+}_{0.40}Al_{0.12}Fe^{3+}_{0.03}Ti^{4+}_{0.04})_{\sum 1.12}P_{1.95}O_7$. This can be simplified to the formula KVP_2O_7, indicating that it may be

https://doi.org/10.1180/mgm.2025.27 Published online by Cambridge University Press

another new mineral. The EMPA points of the pyrophosphate analysis are shown in the classification diagram $KCr^{3+}P_2O_7$ – $KAlP_2O_7$ - $KV^{3+}P_2O_7$ (Fig. 4).

Ferromerrillite, $(Na_{0.76}K_{0.14}Sr_{0.01})_{\sum 0.91}(Fe^{2+}_{0.97}Mg_{0.11}Cr^{3+}_{0.09}V^{3+}_{0.02}Al_{0.03})_{\sum 1.22}Ca_{8.91}(P_{6.90}Si_{0.05})_{\sum 6.95}O_{28}$ (Fig. 3a; Table 1, an. 3), known only in meteorites (Britvin et al., 2016), and a phase close in composition to ferroalluaudite $(Na_{0.70}Ca_{0.41}K_{0.15})_{\sum 1.26}(Fe^{2+}_{0.98}Fe^{3+}_{0.88}Cr^{3+}_{0.53}Al_{0.18}V^{3+}_{0.05}Mg_{0.04}Ti^{4+}_{0.01})_{\sum 2.67}(P_{3.05}Si_{0.01})O_{12}$ (Table 1, an. 4), associate with yamhamelachite. Yamhamelachite usually occurs between zones of barringerite II and an inhomogeneous zone of Fe-Cr spinels where chromite grains are embedded in magnetite (Fig. 3, Table 2).

Zonal phosphide aggregates are represented by early homogeneous barringerite I (*P*-62*m*, *a* = 5.8649(4), c = 3.4625(4) Å) with minor impurities of Cr and V (Table 3, an. 1), which is replaced by rather rare schreibersite-barringgerite eutectics in this breccia (Fig. 3b). In eutectic formations, Cr and V tend to accumulate in barringerite (Table 3, an. 2, 3). In contrast, in schreibersite with few barringerite and coghenite inclusions (Fig. 3b), Cr and V are concentrated in small daubreélite inclusions with the composition $Fe(Cr^{3+}_{1.4}V^{3+}_{0.6})_{\sum 2}S_4$ (EDS data). Barringerite II (*P*-62*m*, *a* = 5.8465(4), *c* = 3.48176(19) Å) which replaces schreibersite, is characterised by low Cr and V content. The effects of the replacement of early phosphides by later ones with higher P content is observed in other fragments of the studied sample, in which yamhamelachite can be found. Specifically, there is a replacement of schreibersite by late barringerite in eutectic schreibersite-barringerite (Fig. 5a, b; Table 4) and a replacement of barringerite by murashkoite with pyrrhotite inclusions (Fig. 5c, d; Table 5).

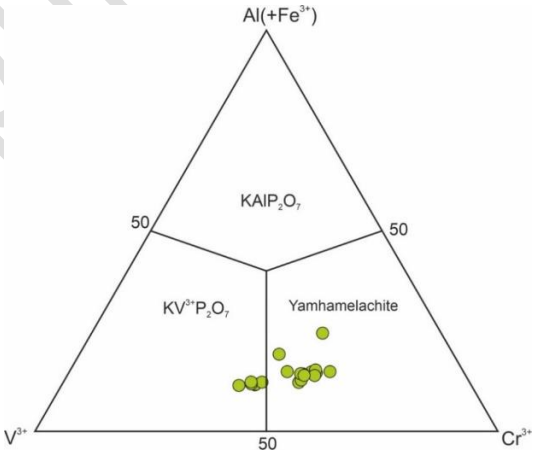

Figure 4. Points of analysis of K-pyrophosphates in the V-Cr-Al ternary diagram.

https://doi.org/10.1180/mgm.2025.27 Published online by Cambridge University Press

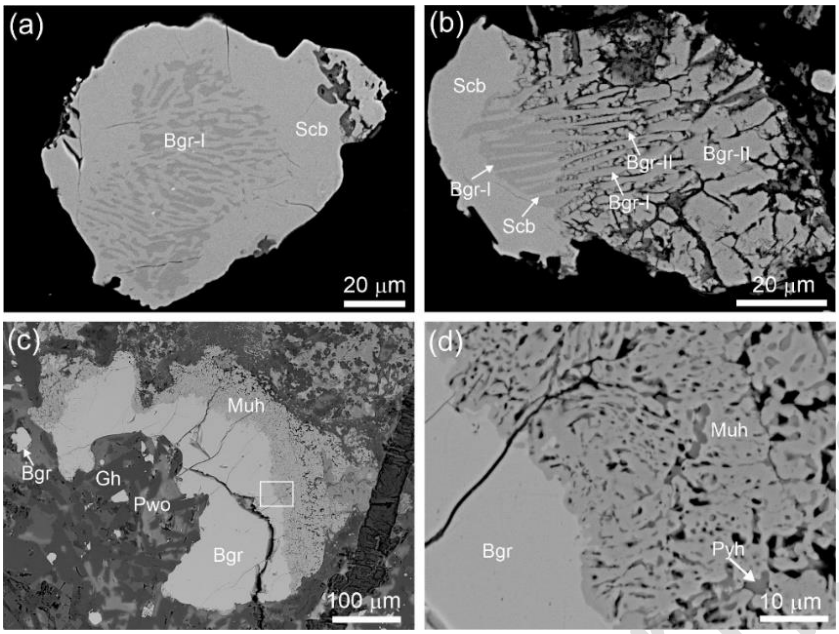

Figure 5. (a) Eutectic of schreibersite-barringerite with schreibersite rim. (b) Grain similar to that shown in Fig. 5a, in which some of the schreibersite in the eutectic is replaced by later barringerite. (c) Barringerite grain with reaction rim of murashkoite. Fragment magnified in Fig. 5d is shown in the frame. (d) Sulfide inclusions are observed in porous murashkoite. Bgr-I – barringerite, generation I; Bgr-II – barringerite, generation II; Dbr – daubréelite, Gh – gehlenite; Hem – hematite; Hgr – hydrogrossular, Muh – murashkoite, Pyh – pyrrhotite, Pwo – pseudowollastonite, Scb – schreibersite.

Table 1. Chemical composition of yamhamelachite (1,2), V-analog of yamhamelachite (3), ferromerrillite (4) and ferroalluaudite (5)

	1			2	3	4			5		
wt.%	n=12	s.d.	range	n=1	n=1	n=12	s.d.	range	n= 6	s.d.	
P_2O_5	53.63	0.34	53.12-54.16	52.46	53.07	43.78	0.39	43.37-44.49	45.82	0.38	45.36-46.55
TiO_2	1.03	0.32	0.56-1.88	0.83	1.32	0.00	0.07	0-0.29	0.15	0.05	0.06-0.22
SiO_2	0.07	0.04	0.01-0.15	n.d.	0.00	0.26	0.19	0.10-0.67	0.11	0.03	0.06-0.17
Cr_2O_3	14.51	1.48	11.83-16.43	16.43	11.59	0.59	0.56	0.05-1.40	8.59	0.13	8.33-8.76
V_2O_3	9.54	2.14	7.65-15.29	9.68	15.29	0.15	0.12	0.06-0.54	0.90	0.17	0.72-1.27
Al_2O_3	2.92	0.60	2.37-4.97	2.81	2.32	0.13	0.08	0.06-0.37	1.97	0.19	1.62-2.29
Fe_2O_3	1.09	0.24	0.71-1.64	1.15	0.79				14.91	0.95	10.89-16.15
FeO	0.00				0.00	6.24	0.25	5.93-6.86	14.86	1.93	11.24-18.63
SrO	0.00	0.01	0-0.02	n.d.	0.00	0.14	0.04	0.07-0.19			
CaO	0.26	0.20	0.08-0.72	0.24	0.08	44.67	0.25	43.97-45.11	4.87	0.95	3.97-6.99
MgO	0.00	0.01	0-0.03	n.d.	0.00	0.41	0.24	0.10-0.70	0.32	0.02	0.31-0.34
K_2O	16.02	0.34	15.35-16.59	16.15	15.65	0.58	0.04	0.50-0.66	1.52	0.28	0.97-1.81
Na_2O	n.d.			n.d.	n.d.	2.09	0.05	1.98-2.16	4.56	0.74	2.80-5.16
Total	99.07			99.75	100.11	99.06			99.43		
				Calculated on 7O*, 28O** and 12O***							
K apfu	*0.89			*0.90	*0.87	**0.14			***0.15		
Na						0.76			0.70		
Ca	0.01			0.01		8.91			0.41		
Sr						0.01					
Mg						0.11			0.04		
Fe^{2+}						0.97			0.98		
Cr^{3+}	0.50			0.57	0.40	0.09			0.53		
V^{3+}	0.33			0.34	0.53	0.02			0.05		
Ti^{4+}	0.03			0.03	0.04				0.01		
Fe^{3+}	0.04			0.04	0.03				0.88		
Al	0.15			0.14	0.12	0.03			0.18		
P	1.98			1.94	1.95	6.90			3.05		

https://doi.org/10.1180/mgm.2025.27 Published online by Cambridge University Press

Si		0.05	0.01

n.d. – not detected

Table 2. Chemical composition (wt.%) of chromite (1) and magnetite (2)

	1			2		
wt.%	n=7	s.d.	range	n=6	s.d.	range
SiO_2	0.27	0.15	0.16-0.54	0.24	0.08	0.14-0.38
Al_2O_3	0.37	0.22	0.07-0.64	0.14	0.11	0.02-0.34
CaO	0.58	0.17	0.28-0.75	0.40	0.17	0.21-0.63
Cr_2O_3	44.41	3.87	39.80-50.43	2.28	1.49	1.32-5.25
V_2O_3	16.63	2.41	11.32-17.06	0.86	0.67	0.44-2.20
TiO_2	0.69	0.39	0.26-1.42	0.07	0.05	0.04-0.17
Fe_2O_3	4.57	0.42	2.88-5.22	64.02	2.65	58.85-66.15
FeO	32.41	2.09	29.02-34.45	30.59	0.25	30.32-30.90
Total	99.93			98.60		
	Calculated on 4O					
Fe^{2+}apfu	1.01			0.99		
Cr^{3+}	1.30			0.07		
V^{3+}	0.49			0.03		
Fe^{3+}	0.13			1.87		
Al	0.02			0.01		
Ca	0.02			0.02		
Ti^{4+}	0.02			0.00		

Table 3. Phosphide chemical compositions from aggregate with yamhamelachite, wt.%: 1 – barringerite I; 2,3 – eutectic: schreibersite (2) – barringerite (3); 4 – barringerite II

	1			2			3			4		
wt.%	n=7	s.d.	range	n = 7	s.d.	range	n = 6	s.d.	range	n = 7	s.d.	range
Si	0.09	0.01	0.08-0.10	0.12	0.02	0.10-0.15	0.11	0.01	0.09-0.12	0.14	0.05	0.11-0.27
P	21.85	0.13	21.64-22.07	15.80	0.09	15.63-15.93	21.67	0.55	21.04-22.27	21.68	0.16	21.43-21.94
S	0.19	0.08	0.09-0.34	0.03	0.01	0.03-0.05	0.06	0.01	0.05-0.09	0.19	0.04	0.10-0.23
Cu	0.02	0.03	0-0.10	0.03	0.02	0-0.06	0.03	0.03	0.00-0.07	0.03	0.03	0.00-0.06
Ni	0.27	0.03	0.24-0.35	0.26	0.02	0.23-0.29	0.29	0.02	0.26-0.33	0.42	0.04	0.36-0.47
Fe	74.25	0.62	72.86-74.95	82.49	0.19	82.13-82.81	70.58	2.39	67.82-75.08	76.47	0.49	75.35-76.92
Cr	2.14	0.53	1.50-3.24	0.69	0.14	0.41-0.86	4.54	0.82	3.19-5.56	0.52	0.13	0.33-0.73
V	1.13	0.11	0.96-1.29	0.22	0.05	0.14-0.28	2.54	0.72	1.67-3.80	0.21	0.07	0.13-0.32
Ti	0.02	0.01	0-0.03	0.00	0.01	0-0.02	0.14	0.07	0.02-0.24	0.01		
Total	99.98			99.64			99.96			99.67		
Fe apfu	1.89*			2.93**			1.79*			1.95*		
Cr	0.06			0.03			0.13			0.01		
V	0.03			0.01			0.07			0.01		
Ni	0.01			0.01			0.01			0.01		
M	***1.99***			***2.98***			***2.00***			***1.98***		
P	1.00			1.01			0.99			1.00		
Si				0.01			0.01			0.01		
S	0.01									0.01		
X	***1.01***			***1.02***			***1.00***			***1.02***		

* - calculated on 3 atoms, ** - calculated on 4 atoms

Table 4. Composition of barringerite-schreibersite grains shown in Fig. 5b: barringerite (2) – schreibersite intergrowth and schreibersite rim (1), secondary barringerite after schreibersite (3).

1	2	3

wt.%	n=6	s.d	range	n=6	s.d.	range	n=6	s.d.	range
Fe	82.25	0.28	81.84-82.68	72.83	0.84	71.25-73.69	74.94	0.56	73.86-75.67
Ni	0.95	0.02	0.90-0.98	1.24	0.04	1.18-1.29	1.15	0.15	0.99-1.44
Cr	0.45	0.10	0.35-0.65	2.98	0.42	2.44-3.63	1.11	0.19	0.74-1.30
V	0.12	0.02	0.10-0.15	0.91	0.25	0.59-1.33	0.31	0.05	0.23-0.39
Cu	0.10	0.04	0.05-0.17	n.d.			n.d.		
Ca	0.27	0.08	0.17-0.38	0.08	0.03	0.05-0.11	0.08	0.03	0.04-0.11
P	15.72	0.03	15.67-15.76	21.71	0.12	21.53-21.91	21.31	0.79	19.61-21.89
S	0.04	0.00	0.04-0.05	0.09	0.01	0.08-0.11	0.26	0.44	0.05-1.24
Si	0.10	0.03	0.06-0.14	0.06	0.02	0.04-0.09	0.14	0.03	0.10-0.17
Total	100.00			99.90			99.30		
				Calculated on 4* and 3** atoms					
Fe apfu	2.92*			1.86			1.92		
Ni	0.03			0.03			0.03		
Cr	0.02			0.08			0.03		
V				0.03			0.01		
Ca	0.01								
P	1.00			1.00			0.99		
S							0.01		
Si	0.01						0.01		

Table 5. Chemical composition of grain shown in Fig. 5d: barringerite (1) with reaction rim of porous murashkoite (2) with pyrrotite inclusions (3)

		1			2		3
wt.%	*n* = 11			*n* = 13			*n* = 4
Fe	71.56	0.67	70.26-73.20	61.80	1.97	56.90-63.80	58.13
Ni	0.67	0.34	0.39-1.60	0.62	0.34	0.11-1.38	0.31
Cr	4.11	0.53	2.51-4.45	1.13	0.97	0.20-3.87	1.07
V	1.66	0.16	1.28-1.83	0.53	0.49	0.10-2.03	0.46
Ca	0.00	0.02	0.01-0.09	0.04	0.03	0-0.13	0.14
P	21.84	0.07	21.74-22.01	33.40	1.82	29.27-35.40	
S	0.08	0.02	0.06-0.14	2.48	1.98	0.21-6.50	39.52
Si	0.04	0.01	0.03-0.07	0.08	0.05	0.03-0.18	
Total	99.97			100.07			99.63
				Calculated on 3* and 2** atoms			
Fe apfu	1.82*			0.96**			0.85**
Ni	0.02			0.01			0.00
V	0.05			0.01			0.01
Cr	0.11			0.02			0.02
P	1.00			0.93			0.00
S	0.00			0.07			1.00

Raman spectroscopy and structure of yamhamelachite

The Raman spectrum of yamhamelachite is similar to that of its synthetic analogue (Elouafi *et al.*, 2023). The following bands are observed in the yamhamelachite spectrum (Fig. 6, cm^{-1}): $\nu_{as}(PO_2)$ - 1260, 1222; $\nu_{s}(PO_2)$ - 1190, 1134, 1102; $\nu_{as}(POP)$ - 1059, 1025, 917;

https://doi.org/10.1180/mgm.2025.27 Published online by Cambridge University Press

ν_s(POP) – 775; δ(PO_2) - 608, 588, 564; δ(POP) - 478, 441, 423, 365; T(Cr,V) – 234; T(K) – 194; T(P_2O_7) + L - 152, 117. Data from previous studies of Raman spectra of various pyrophosphates (Corlinsen and Condrate, 1977; Stranford *et al*., 1981; Corlinsen, 1984; Szczygieł *et al*., 2007; Capitilli *et al*., 2007; El Arni *et al*., 2023) informed the band assignments.

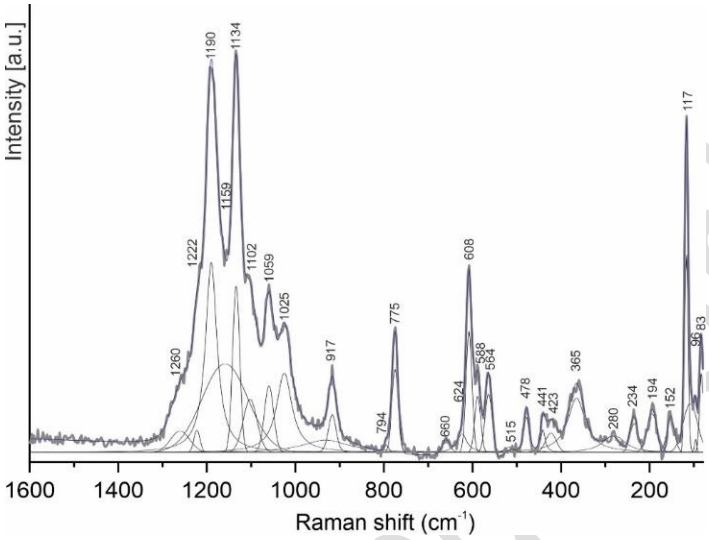

Figure 6. Raman spectrum of yamhamelachite.

Single-crystal X-ray diffraction data were collected for a small yamhamelachite crystal fragment (30×10×8 μm) using a SuperNova diffractometer. The predominance of Cr over V was confirmed by semi-quantitative analysis of selected grains using EDS/SEM. The structure of yamhamelachite was refined using the SHELX-2019/2 program (Sheldrick, 2015). Its crystal structure was refined from the atomic coordinates of synthetic $KCrP_2O_7$ (Gentil *et al*., 1997). Experimental details and refinement data are summarized in Tables 6–9. The structure of yamhamelachite ($P2_1/c$, a = 7.3574(3) Å, b = 9.9336(4) Å, c = 8.1540(4) Å, β = 106.712(5)°, V = 570.77(5) $Å^3$, Z = 4) is shown in Fig. 7a–c. It can be described as layered, with single layers formed by Cr^{3+}(V^{3+})-octahedra connected by $(P_2O_7)^{4-}$ groups (Fig. 7d), and as consisting of columns of octahedra and pyrophosphate groups (Fig. 7e). In the $(P_2O_7)^{4-}$ group, the two corner-linked PO_4 tetrahedra are slightly distorted as might be expected, where the linking (P1,P2-O4) distances both being ~1.61 Å while the remaining three P-O distances are ~1.49-1.52 Å in each case. The $(P_2O_7)^{4-}$ group is significantly bent with a dihedral angle for the (P1-O4-P2) bond of 124.09(11), which is due to the $(P_2O_7)^{4-}$ group being able to act as a bidentate ligand, forming a 6-membered chelate ring with Cr^{3+} via bonds to O1 and O6 (both ~1. 52 Å), while acting as a monodentate ligand for the remaining four O atom positions of the $(CrO_6)^{9-}$ coordination octahedron (Fig. 7d, Table 9).

https://doi.org/10.1180/mgm.2025.27 Published online by Cambridge University Press

Interestingly, the $(CrO_6)^{9-}$ octahedron is only slightly distorted even in the presence of significant V^{3+} and Al^{3+} replacing Cr^{3+} in the central metal site. The resulting structure, which can be described as a 3D covalent lattice formed by the corner bonding of $(CrO_6)^{9-}$ octahedra and $(P_2O_7)^{4-}$ pyrophosphate groups, results in open channels parallel to [001], which can then accommodate the K cations in large 10-coordinate sites, if K-O distances of up to 3.22 Å are considered viable contacts (Fig. 7c, Table 9).

The structural formula of yamamelachite $K_{0.953}(Cr_{0.77}Al_{0.23})P_2O_7$ is close to the empirical formula $(K_{0.89}Ca_{0.01}\square_{0.10})_{\sum 1.00}Cr^{3+}_{0.50}V^{3+}_{0.33}Al_{0.15}Fe^{3+}_{0.04}Ti^{4+}_{0.03})_{\sum 1.05}P_{1.98}O_7$ (Tables 1, 6). The resulting K- and Cr-site occupancies give site-scattering values of 18.11 and 21.47 epfu (structural formula) and 17.11 and 23.24 epfu (empirical formula), respectively. It is likely that the grain used for structural studies contained more Al than the calculated average Al content (Table 1, an.1).

Table 6. Crystal data and structure refinement details for yamhamelachite

Crystal data	
Formula from refinement	$K_{0.953}Cr_{0.77}Al_{0.23}P_2O_7$
Crystal system	monoclinic
Space group	$P2_1/c$ (no. 14)
Unit-cell dimensions	a = 7.3574(3)Å b = 9.9336(4) Å c = 8.1540(4)Å β = 106.712(5)° V = 570.77(5)Å^3
Z	4
Absorption coefficient	25.056 mm^{-1}
F(000)	502
Crystal size	0.03 × 0.01 × 0.008 mm^3
Data collection	
Diffractometer	SuperNova with Atlas CCD
Radiation wavelength	Cu$K\alpha$, λ = 1.54184 Å
min. & max. theta	6.28°, 73.21°
Reflection ranges	$-8 \le h \le 8$; $-12 \le k \le 8$; $-8 \le l \le 10$
Refinement of structure	
Reflection measured	3945
No. of unique reflections	1121
No. of observed unique refl. [$I>2\sigma(I)$]	1029
Refined parameters	102
Rint	0.0238
R_1 / R_{all}	0.0246/0.0276
w$R(F^2)$*	0.0674
Goof	1.072
$\Delta\rho_{min}$ [e Å^{-3}]	-0.498
$\Delta\rho_{max}$ [e Å^{-3}]	0.320

* Weighting scheme: $w = 1/[\sigma^2(F_o^2) + (0.0427P)^2 + 0.1098P]$, where $P = (F_o^2 + 2F_c^2)/3$

https://doi.org/10.1180/mgm.2025.27 Published online by Cambridge University Press

Table 7. Atomic coordinates, equivalent-isotropic displacement parameters (Å^2) and site occupancy (Occ) for yamhamelachite

site	atom	*x*	*y*	*z*	U_{eq}	Occ.
Cr1	Cr	0.73532(6)	0.10043(4)	0.76127(5)	0.00719(17)	0.770(6)
Al1	Al	0.73532(6)	0.10043(4)	0.76127(5)	0.00719(17)	0.230(6)
P1	P	0.63257(9)	0.09627(6)	0.33074(8)	0.01018(18)	1
P2	P	0.94108(9)	0.13621(6)	0.19143(8)	0.01033(18)	1
O1	O	0.9513(3)	0.28355(18)	0.2430(2)	0.0147(4)	1
O2	O	0.1391(3)	0.07790(18)	0.2334(2)	0.0163(4)	1
O3	O	0.8211(3)	0.10680(19)	0.0121(2)	0.0190(4)	1
O4	O	0.8388(3)	0.05794(18)	0.3133(2)	0.0151(4)	1
O5	O	0.5039(3)	0.00494(18)	0.7782(2)	0.0133(4)	1
O6	O	0.5828(3)	0.26430(18)	0.7540(2)	0.0141(4)	1
O7	O	0.6444(3)	0.0910(2)	0.5160(2)	0.0181(4)	1
K1	K	0.32104(9)	0.32025(7)	0.44611(8)	0.0223(2)	0.953(4)

Table 8. Anisotropic displacement parameters (Å^2)

	U^{11}	U^{22}	U^{33}	U^{23}	U^{13}	U^{12}
Cr1	0.0067(3)	0.0082(3)	0.0068(3)	-0.00017(15)	0.00198(17)	-0.00033(16)
Al1	0.0067(3)	0.0082(3)	0.0068(3)	-0.00017(15)	0.00198(17)	-0.00033(16)
P1	0.0100(3)	0.0115(3)	0.0096(3)	-0.0001(2)	0.0037(2)	-0.0008(2)
P2	0.0087(3)	0.0116(3)	0.0110(3)	-0.0001(2)	0.0033(2)	0.0003(2)
O1	0.0124(9)	0.0136(10)	0.0183(9)	-0.0019(7)	0.0049(7)	-0.0003(7)
O2	0.0121(10)	0.0161(9)	0.0218(10)	-0.0013(7)	0.0063(7)	0.0018(7)
O3	0.0215(10)	0.0204(10)	0.0136(10)	-0.0009(7)	0.0026(8)	0.0014(8)
O4	0.0130(9)	0.0159(9)	0.0177(9)	0.0039(7)	0.0066(7)	0.0026(7)
O5	0.0143(9)	0.0139(9)	0.0118(8)	-0.0012(7)	0.0038(7)	-0.0025(7)
O6	0.0123(9)	0.0128(9)	0.0171(9)	-0.0010(7)	0.0037(7)	-0.0007(7)
O7	0.0198(10)	0.0235(10)	0.0123(9)	-0.0011(7)	0.0064(7)	-0.0057(7)
K1	0.0196(4)	0.0264(4)	0.0191(4)	-0.0013(2)	0.0025(2)	-0.0009(2)

Table 9. Selected bond lengths (Å) and BVS* calculations for yamhamelachite

atom	-atom	distance	atom	-atom	distance
Cr1	O7	1.9199(19)	K1	O1	2.7722(19)
	O3	1.960(2)		O2	3.0432(19)
	O6	1.9683(18)		O2	3.179(2)
	O5	1.9883(19)		O3	3.085(2)
	O2	1.9927(18)		O4	3.162(2)
	O1	2.0026(19)		O5	2.7857(19)
	mean	1.972		O5	2.9009(19)
	BVS	3.05		O6	2.7460(19)
P1	O7	1.4889(19)		O6	2.9330(19)
	O5	1.5147(18)		O7	3.224(2)
	O6	1.5205(18)		mean	2.983
	O4	1.6098(19)		BVS	1.11
	mean	1.533		O1 BVS	1.95
	BVS	5.05		O2	1.95
P2	O3	1.503(2)		O3	1.96
	O2	1.5126(19)		O4	2.10
	O1	1.5189(19)		O5	2.10
	O4	1.6087(19)		O6	2.11
	Mean	1.536		O7	2.06
	BVS	5.01	P2 - O4 - P1 = 124.09(11)°		

*- Calculated using ECoN21 (Ilinca, 2022)

https://doi.org/10.1180/mgm.2025.27 Published online by Cambridge University Press

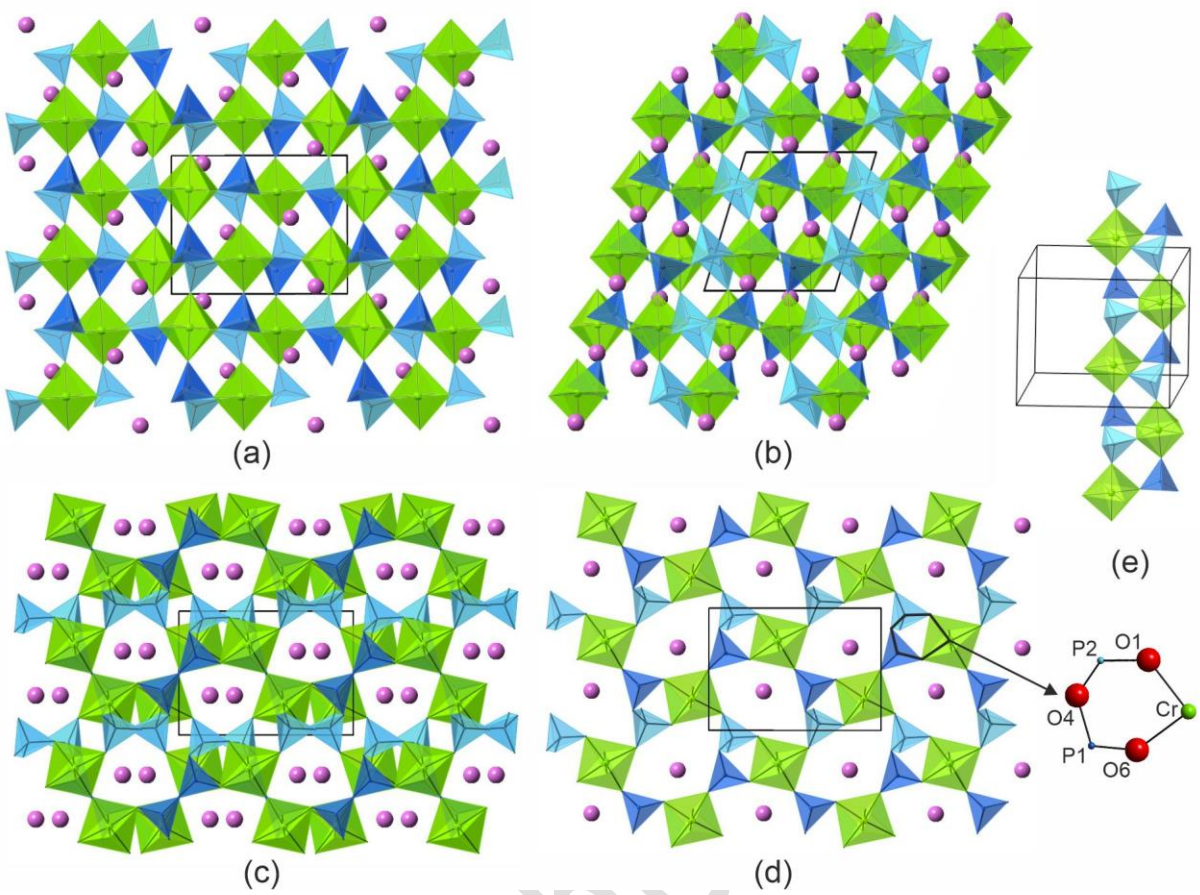

Figure 7. The structure of yamhamelachite: (a) Projection on (100). (b) Projection on (010). (c) Projection on (001). (d) For the projection on (001), only one structural layer is shown. Chelate ring is shown. (e) Columns in yamhamelachite formed by pyrophosphate groups $(P_2O_7)^{4-}$ and octahedra $[(Cr,V)O_6]^{9-}$. Green octahedra – $[(Cr,V)O_6]^{9-}$, dark-blue tetrahedra – ($P1O_4$), light-blue tetrahedra – ($P2O_4$), pink balls – K.

Discussion

The formation of phosphides at the contact between heated paralava and clinkered sedimentary rock fragments of the Ghareb Formation containing graphitised fishbone remnants and oxidised pyrite framboids has been associated with carbothermal reduction processes (Galuskin *et al*., 2023b,2024a). Partial contamination of melt by clinkered sedimentary rock fragments resulted in the concentration of iron droplets in the contact facies of the paralava. These droplets absorbed gaseous phosphorus, which was reduced in the pyrometamorphic process, leading to the formation of phosphides. The usual sequence of phosphide crystallisation in the gehlenite paralava contact facies is barringerite → schreibersite → eutectic: schreibersite-iron, indicating a reduction in phosphorus activity (Galuskin *et al*., 2022).

However, there are local manifestations of an increase in phosphorus activity in the system, reflected in the replacement of schreibersite (Fe_3P) by barringerite (Fe_2P) and in the

https://doi.org/10.1180/mgm.2025.27 Published online by Cambridge University Press

formation of reaction rims of murashkoite (FeP) on barringerite (Fe_2P) (Figs. 3b, 5). The pyrometamorphic process (combustion) is not stationary; relatively abrupt changes in temperature, composition and the reduction-oxidation properties of the system occur over time, associated with the realisation of the process exclusively on the surface or in the near-surface zones of the Earth. Yamhamelachite is formed where there is a repeated local increase in phosphorus activity, as indicated by the occurrence of barringerite II and murashkoite (Figs. 3b, 5).

Further evolution of the process proceeds with increasing oxygen activity, as phosphides are replaced by phosphates and oxides (Fig. 3a). We believe that the insignificant Fe^{3+} admixture in yamhamelachite detected by the microprobe analyzer is associated with late processes of mass hematisation of rocks (Fig. 2d). Yamhamelachite crystallised in the oxygen fugacity interval between the buffers IW (iron/wustite) and WM (wustite/magnetite), and the high V^{3+} content in the mineral indicates that the log f_{O2} Δ(IW) approached 0 (Papike *et al.*, 2013).

Yamhamelachite is a high-temperature mineral and, like associated minerals of the merrillite subgroup, crystallised at a temperature of ~1000°C from small portions of phosphate melt (Britvin *et al.*, 2023; Galuskin *et al.*, 2023c, 2024b). The distinctive feature of mineral crystallisation from a melt formed during pyrometamorphic processes is the anhydrous nature of the melt and its possible local purging with high temperature gases of different compositions. Crystallisation of yamhamelachite, a pyrophosphate with a large cation (K) in the channels of the structure, took place from a high-temperature phosphate melt under low pressure conditions. The source of Cr and V for yamhamelachite was sulfides (daubreélite, pyrrhotite) and, to a lesser extent, phosphides. The formation of natural pyrophosphates and cyclophosphates in pyrometamorphic rocks of the Hatrurim Complex was only possible by crystallisation from small portions of reduced phosphate melt, which determined the polymerisation of (PO_4)-tetrahedra and the absence of Fe^{3+} in these minerals.

Acknowledgments: The authors would like to thank Sergey Britvin, Peter Leveret and Igor Pekov for their comments and suggestions that improved an earlier version of the manuscript. Investigations were partially supported by the National Science Centre of Poland Grant No. 2021/41/B/ST10/00130.

Conflicts of Interest: The authors declare no conflict of interest.

https://doi.org/10.1180/mgm.2025.27 Published online by Cambridge University Press

References

Bentor Y.K. (editor) (1960) Israel. In: Lexique Stratigraphique International, Asie, Vol. III, (10.2). Centre national de la recherche scientifique, Paris.

Brese, N.E. and O'Keeffe, M.O. (1991) Bond-valence parameters for solids. *Acta Crystallographica*, **B47**, 192-197.

Brown, I.D. and Altermatt, D. (1985) Bond-valence parameters obtained from a systematic analysis of the Inorganic Crystal Structure Database. *Acta Crystallographica*, **B41**, 244-247.

Britvin, S.N., Murashko M.N., Vapnik Y., Polekhovsky and Yu.S., Krivovichev, S.V. (2015) Earth's Phosphides in Levant and insights into the source of Archean prebiotic phosphorus. *Scientific Reports*, **5**, 8355. https://doi.org/10.1038/srep08355

Britvin, S.N., Krivovichev, S.V. and Armbruster, T. (2016) Ferromerrillite, $Ca_9NaFe^{2+}(PO_4)_7$, a new mineral from the Martian meteorites, and some insights into merrillite–tuite transformation in shergottites. *European Journal of Mineralogy*, **28**, 125–136.

Britvin, S.N., Murashko, M.N., Vapnik, Y., Vlasenko, N.S., Vereshchagin, O.S., Bocharov, V.N., Krzhizhanovskaya, M.G., Lozhkin, M.S. and Zolotarev, A.A. (2020a) Anastasenkoite, IMA 2020-026. CNMNC Newsletter No. 56; *Mineralogical Magazine*, **84**, https://doi.org/10.1180/mgm.2020.60

Britvin, S.N., Murashko, M.N., Vapnik, Y., Vlasenko, N.S., Vereshchagin, O.S. and Bocharov, V.N. (2021a) Lisanite, IMA 2021-014. CNMNC Newsletter 61; *Mineralogical Magazine*, **85**, https://doi.org/10.1180/mgm. 2021.48

Britvin, S.N., Murashko, M.N., Vapnik, Y., Vlasenko, N.S., Vereshchagin, O.S., Krzhizhanovskaya, M.G. and Bocharov, V. N. (2021b) Shasuite, IMA 2021-020, in: CNMNC Newsletter 62, *European Journal of Mineralogy*, **33**, https://doi.org/10.5194/ejm-33-479-2021.

Britvin, S.N., Murashko, M.N., Vapnik, Y., Vlasenko, N.S., Vereshchagin, O.S., Krzhizhanovskaya, M.G. and Bocharov, V. N. (2021c) Nabateaite, IMA 2021-026, in: CNMNC Newsletter 62, *European Journal of Mineralogy*, **33**, https://doi.org/10.5194/ejm-33-479-2021.

Britvin, S.N., Murashko, M.N., Vereshchagin, O.S., Vapnik, Y., Vlasenko, N.S., Krzhizhanovskaya, M.G. and Bocharov, V. N. (2021d) Samraite, IMA 2021-029, in: CNMNC Newsletter 62, *European Journal of Mineralogy*, **33**, https://doi.org/10.5194/ejm-33-479-2021.

Britvin, S.N., Murashko, M.N., Vapnik, Y., Vlasenko, N.S., Krzhizhanovskaya, M.G., Vereshchagin, O.S., Bocharov, V.N. and Lozhkin, M.S. (2021e) Cyclophosphates, a new class of native phosphorus compounds, and some insights into prebiotic phosphorylation on early Earth. *Geology*, **49**, 382–386.

Britvin S.N., Murashko M.N., Krzhizhanovskaya M.G., Vlasenko N.S., Vereshchagin O.S., Vapnik Ye. and Bocharov V.N. (2023) Crocobelonite,$CaFe^{3+}_2(PO_4)_2O$, a new oxyphosphate mineral, the product of pyrolytic oxidation of natural phosphides. *American Mineralogist*, **108**, 1973–1983.

Capitelli, F., Dridi, N., Arbib, E.H., Valentini, V. and Mattei, G. (2007) New monodiphosphate $Li_9Cr_3(P_2O_7)_3(PO_4)_2$: X-ray crystal structure and vibrational spectroscopy. *Zeitschrift für Kristallographie*, **222**, 521–526.

Cornilsen, B.C. (1984) Solid state vibrational spectra of calcium pyrophosphate dihydrate. *Journal of Molecular Structure*, **117**, 1–9.

El Arni, S., Hadouchi, M., Assani, A., Saadi, M., El Marssi, M., Lahmar, A. and El Ammari, L. (2023) Structural and magnetic investigations of the novel pyrophosphate $Na_7Ni_3Fe(P_2O_7)_4$. *Magnetochemistry*, **9**, 162.

Elouafi, A., Ouahbi, S.E., Ezairi, S., Lmai, F., Tizliouine, A. and Lassri, H. (2023) Structural, Magnetic, and magnetocaloric studies of the potassium diphosphate $KCrP_2O_7$. *Journal of Superconductivity and Novel Magnetism*, **36**, 521–528.

Galuskin, E. and Galuskina, I. (2023) Evidence of the anthropogenic origin of the 'Carmel sapphire' with enigmatic super-reduced minerals. *Mineralogical Magazine*, **87**, 619–630.

Galuskin, E., Galuskina, I.O., Kamenetsky, V., Vapnik, Y., Kusz, J. and Zieliński, G. (2022) First *In Situ* Terrestrial osbornite (TiN) in the pyrometamorphic Hatrurim Complex, Israel. *Lithosphere*, **2022**, 8127747.

Galuskin, E.V., Galuskina, I.O., Vapnik, Y. and Zieliński, G. (2023a) Discovery of "Meteoritic" layered disulphides $ACrS_2$ (A = Na, Cu, Ag) in terrestrial rock. *Minerals*, **13**, 381.

Galuskin, E.V., Kusz, J., Galuskina, I.O., Książek, M., Vapnik, Y. and Zieliński, G. (2023b) Discovery of terrestrial andreyivanovite, FeCrP, and the effect of Cr and V substitution on the low-pressure barringerite-allabogdanite transition. *American Mineralogist*, **108**, 1506–1515.

Galuskin E.V., Stachowicz M., Galuskina I.O., Woźniak K., Vapnik Y., Murashko M.N., Zieliński G. (2023c) Deynekoite, $Ca_9□Fe^{3+}(PO_4)_7$ - A new mineral of the merrillite

https://doi.org/10.1180/mgm.2025.27 Published online by Cambridge University Press

group from phosphide-bearing contact facies of paralava, Hatrurim Complex,Daba-Siwaqa. Jordan. *Mineralogical Magazine*, **87**, 943–954.

Galuskin, E., Galuskina, I., Vapnik, Y., Kusz, J., Marciniak-Maliszewska, B. and Zieliński, G. (2024a) Two modes of terrestrial phosphide formation. *American Mineralogist*, https://doi.org/10.2138/am-2024-9315.

Galuskin E.V., Galuskina I.O., Kusz J., Książek M., Vapnik Y., Zieliński, G. (2024b) Karwowskiite, $Ca_9(Fe^{2+}0.5□0.5)Mg(PO_4)_7$ - A new merrillite group mineral from paralava of the Hatrurim Complex, Daba-Siwaqa, Jordan. *Minerals*, **14**, 825.

Galuskina, I.O., Galuskin, E.V., Pakhomova, A.S., Widmer, R., Armbruster, T., Krüger, B., Grew, E.S., Vapnik, Y., Dzierżanowski, P. and Murashko, M. (2017) Khesinite, $Ca_4Mg_2Fe^{3+}{}_{10}O_4[(Fe^{3+}{}_{10}Si_2)O_{36}]$, a new rhönite-group (sapphirine supergroup) mineral from the Negev Desert, Israel– natural analogue of the SFCA phase. *European Journal of Mineralogy*, **29**, 101–116.

Gentil, S., Andreica, D., Lujan, M., Rivera, J.-P., Kubel, F. and Schmid, H. (1997) Synthesis, structure and magnetic susceptibility of $KCrP_2O_7$, a potential antiferromagnetic magnetoelectric. *Ferroelectrics*, **204**, 35–44.

Gross S. (1977) The mineralogy of the Hatrurim Formation, Israel. Geological Survey of Israel Bulletin, **70**, 1–80.

Huminicki D. M.C. and Hawthorne F.C. (2002) The crystal chemistry of the phosphate minerals. *Reviews in Mineralogy and Geochemistry*, **48**, 123–253

Ilinca, G. (2022) Charge Distribution and Bond Valence Sum Analysis of Sulfosalts—The ECoN21 Computer Program. Minerals **2022**, 12, 924.

Ng, H.N. and Calvo, C. (1973) The crystal Structure of $KAlP_2O_7$. *Canadian Journal of Chemistry*, **51**, 2613–2620.

Novikov, I., Vapnik, Y. and Safonova, I. (2013) Mud volcano origin of the Mottled Zone, South Levant. *Geoscience Frontiers*, **4**, 597–619.

Papike, J.J., Burger, P.V., Bell, A.S., Le, L., Shearer, C.K., Sutton, S.R., Jones, J. and Newville, M. (2013) Developing vanadium valence state oxybarometers (spinel-melt, olivine-melt, spinel-olivine) and V/(Cr+Al) partitioning (spinel-melt) for martian olivine-phyric basalts. *American Mineralogist*, **98**, 2193–2196.

Sheldrick, G.M. (2015) Crystal structure refinement with *SHELXL*. *Acta Crystallographica Section C Structural Chemistry*, **71**, 3–8.

Szczygieł, I., Macalik, L., Radomińska, E., Znamierowska, T., Mączka, M., Godlewska, P. and Hanuza, J. (2007) Luminescence, electronic absorption and vibrational IR and

Raman studies of binary and ternary cerium ortho-, pyro- and meta-phosphates doped with Pr^{3+} ions. *Optical Materials*, **29**, 1192–1205.

Vapnik Y., Sharygin V.V., Sokol E.V. and Shagam R. (2007) Paralavas in a combustion metamorphic complex: Hatrurim Basin, Israel. *Reviews in Engineering Geology*, **18**, 1–21.

https://doi.org/10.1180/mgm.2025.27 Published online by Cambridge University Press